Available online at www.sciencedirect.com
ScienceDirect
International Journal of Heat and Fluid Flow 28 (2007) 1034–1048
International Journal of HEAT AND FLUID FLOW
www.elsevier.com/locate/ijhff

Some characteristics of developing bubbly flow in a vertical mini pipe

T. Hibiki [a,*], T. Hazuku [b], T. Takamasa [b], M. Ishii [a]

[a] School of Nuclear Engineering, Purdue University, 400 Central Drive, West Lafayette, IN 47907-2017, USA
[b] Faculty of Marine Technology, Tokyo University of Marine Science and Technology, Koto, Tokyo 135-8533, Japan

Received 2 November 2006; received in revised form 18 January 2007; accepted 22 January 2007
Available online 8 March 2007

Abstract

Accurate prediction of the flow parameters is essential to successful development of the interfacial transfer terms in the two-phase flow formulation in a mini channel. From this point of view, axial measurements of flow parameters such as void fraction, interfacial area concentration, gas velocity, bubble Sauter mean diameter, and bubble number density were performed by the image processing method at five axial locations in vertical upward developing bubbly flows using a 1.02 mm-diameter pipe. The frictional pressure loss was also measured by a differential pressure cell. In the experiment, the superficial liquid velocity and the void fraction ranged from 1.02 m/s to 4.89 m/s and from 0.980% to 24.6%, respectively. The constitutive equation for the drift velocity applicable to mini channel flow was developed by considering the effect of the frictional pressure loss on the drift velocity. The constitutive equation for the distribution parameter was also developed by considering the flow transition from laminar to turbulent flows. The drift-flux model with the modeled constitutive equations for the distribution parameter and drift velocity agreed with the measured void fractions within the averaged prediction accuracy of ±6.76%. The applicability of the existing interfacial area concentration model to mini channel flow was validated by the measured interfacial data.

Keywords: Mini channel; Micro-channel; Interfacial area concentration; Drift-flux model; Bubbly flow; Multiphase flow

1. Introduction

In relation to the cooling of a diverter of a fusion reactor, high power electronic devices and compact heat exchangers, it has become important to understand the characteristics of gas–liquid two-phase flow in a mini channel. In a mini channel, the effect of the axial frictional pressure loss is remarkable and the surface tension force often dominates the gravitational force. For example, the rising velocity of bubbles in stagnant water becomes zero in a capillary tube (Gibson, 1913). Thus, it is anticipated that the characteristics of gas–liquid two-phase flow differ from those in a conventional pipe with a larger inner diameter, which consequently affect the boiling heat transfer. Its engineering importance as well as scientific curiosity has driven the works relevant to the mini channel flow. Reliable and extensive databases and correlations of various flow parameters including void fraction, frictional pressure loss, heat transfer coefficient and critical heat flux are being developed (Lee and Lee, 2001a,b; Kandlikar, 2002a,b; Serizawa et al., 2002; Qu and Mudawar, 2003; Ghiaasiaan, 2003; Kawaji and Chung, 2004; Zhang et al., 2004, 2005, 2006; Ohta, 2005).

In addition to the above works, we emphasize the necessity to address several challenging subjects in a mini channel such as (I) mechanistic modeling of flow parameters, (II) interfacial area concentration measurement, and (III) developing flow measurement to understand the detailed flow characteristics of gas–liquid two-phase flow in the mini channel. Significant axial pressure loss along the flow direction in the mini channel leads to rapid void fraction development within a relatively short distance. Since the axial pressure loss acts as flow-induced body acceleration, we may need to consider the effect of the axial pressure loss

* Corresponding author. Tel.: +1 765 496 9033; fax: +1 765 494 9570.
E-mail address: hibiki@ecn.purdue.edu (T. Hibiki).

0142-727X/$ - see front matter © 2007 Elsevier Inc. All rights reserved.
doi:10.1016/j.ijheatfluidflow.2007.01.001

Nomenclature

a_i	interfacial area concentration, 1/m
C	Chisholm parameter
C_D	drag coefficient for multi-particle system
$C_{D\infty}$	drag coefficient for single-particle system
C_0	distribution parameter
C_∞	asymptotic value of C_0
c	coefficient
D	pipe diameter, m
D_H	hydraulic equivalent diameter of flow channel, m
D_{Sm}	bubble Sauter mean diameter, m
E	absolute deviation from averaged void fraction
f	friction factor
$f(\langle\alpha_g\rangle)$	function
g_z	gravitational acceleration, m/s^2
j	mixture volumetric flux, m/s
j_k	superficial velocity of k phase, m/s
L	pipe length, m
Lo	Laplace length, m
M_{ik}	interfacial force of k phase, N/m^3
M_F	frictional pressure loss gradient of two-phase flow, N/m^3
$M_{F\infty}$	frictional pressure loss gradient of liquid single-phase flow, N/m^3
N	number of processed images
N_{a_i}	non-dimensional interfacial area concentration
$N_{D_{Sm}}$	non-dimensional bubble Sauter mean diameter
N_{Lo}	non-dimensional Laplace length
N_{Re}	Reynolds number defined by Eq. (13)
$N_{Re\infty}$	Reynolds number defined by Eq. (13)
N_{Re_b}	Reynolds number defined by Eq. (29)
N_{Re_f}	Reynolds number
$N_{\mu f}$	viscous number
n_b	bubble number density, 1/m^3
p	pressure, N/m^2
p_m	mixture pressure, N/m^2
r_b	bubble diameter, m
r_b^*	non-dimensional bubble diameter, m
v_g	gas velocity, m/s
v_{gj}	drift velocity, m/s
v_r	relative velocity for multi-particle system, m/s
$v_{r\infty}$	relative velocity for single-particle system, m/s
$v_{r\infty}^*$	non-dimensional relative velocity for single-particle system
X	Martinelli parameter
z	axial coordinate, m

Greek symbols

α_k	volume fraction of k phase
α_{kw}	mean volume fraction of k phase
$\Delta\rho$	density difference, kg/m^3
ε	energy dissipation rate per unit mass, m^2/s^3
μ_k	viscosity of k phase, N s/m^2
μ_m	mixture viscosity, N s/m^2
ν_f	kinematic viscosity of liquid phase, m^2/s
ξ	bubble breakup and coalescence index
ρ_k	density of k phase, kg/m^3
ρ_m	mixture density, kg/m^3
σ	surface tension, N/m
τ_{kw}	wall shear stress of k phase, N/m^2
τ_i	interfacial stress of k phase, N/m^2
Φ_f^2	two-phase friction multiplier
ψ	function

Superscripts

d	downstream
u	upstream

Subscripts

F	friction
g	gas phase
f	liquid phase
f-1ϕ	frictional pressure loss when liquid component flows in pipe as single-phase flow
g-1ϕ	frictional pressure loss when gas component flows in pipe as single-phase flow

on some flow parameters. Also, lack of proper mechanistic models for the interfacial structure and interfacial transfer processes leads to inaccurate predictions of these phenomena, and thus becomes the major concern in the current two-phase flow modeling practice (Ishii and Hibiki, 2005).

As for (I) the mechanistic modeling of flow parameters, empirical correlations are often developed based on available databases. For example, the drift-flux model approach with empirically-determined distribution parameter and drift velocity is commonly adopted for void fraction and gas velocity prediction method. Very few prediction methods are developed based on a rigorous mechanistic modeling approach. Regarding (II) the interfacial area concentration measurement, almost no data of the interfacial area concentration are available in spite of its significance in two-phase flow formulation. This is mainly due to the difficulty to measure the interfacial area concentration in a mini channel with a non-intrusive method. As to (III) the developing flow measurement, very limited data are available in the literature. In many cases, flow measurements in mini channels are performed at a fixed axial location.

From these points of view, this study aims at (i) the mechanistic modeling of drift-flux model applicable to a bubbly flow in a mini channel, (ii) the extensive axial measurement of flow parameters such as void fraction,

interfacial area concentration, gas velocity, bubble Sauter mean diameter and bubble number density and (iii) the evaluation of the interfacial area concentration model obtained in a conventional pipe with data taken in the mini channel. The mini channel utilized in this study is a vertical round pipe with an inner diameter of 1.02 mm. The detailed discussion is made on the axial developments of the flow parameters.

2. Drift-flux model and interfacial area correlation model in mini channel

2.1. One-dimensional drift-flux model

One-dimensional drift-flux model is expressed as (Zuber and Findlay, 1965)

$$\langle\langle v_g\rangle\rangle = \frac{\langle j_g\rangle}{\langle\alpha_g\rangle} = C_0\langle j\rangle + \langle\langle v_{gj}\rangle\rangle, \tag{1}$$

where v_g, j_g, α_g, C_0, j and v_{gj} are, respectively, gas velocity, superficial gas velocity, void fraction, distribution parameter, mixture volumetric flux and drift velocity. $\langle\,\rangle$ and $\langle\langle\rangle\rangle$ indicate area-averaged and void fraction-weighted-mean quantities, respectively. Given the distribution parameter and void fraction-weighted-mean drift velocity defined as Eq. (2), we can predict the area-averaged gas velocity and void fraction from operational parameters such as superficial gas and liquid velocities.

$$C_0 = \frac{\langle\alpha_g\rangle\langle j\rangle}{\langle\alpha_g j\rangle} \quad \text{and} \quad \langle\langle v_{gj}\rangle\rangle = \frac{\langle v_{gj}\alpha_g\rangle}{\langle\alpha_g\rangle}. \tag{2}$$

The constitutive equations for the distribution parameter and drift velocity are given depending on the flow regime and channel (Ishii and Hibiki, 2005; Ishii, 1977).

2.2. Modeling of drift velocity in mini channel

Moving velocity of a single bubble relative to a fully-developed liquid flow in a confined channel can be derived by the momentum equations for the bubble and the liquid flow as (Tomiyama et al., 1998)

$$v_{r\infty}|v_{r\infty}| = \frac{8}{3}\frac{r_b}{C_{D\infty}\rho_f}(\Delta\rho g_z + M_{F\infty}), \tag{3}$$

where $v_{r\infty}$, r_b, $C_{D\infty}$, ρ_f, $\Delta\rho$, g_z and $M_{F\infty}$ are, respectively, relative velocity between bubble and liquid flow, bubble radius, drag coefficient for a single bubble, liquid density, density difference, gravitational acceleration and frictional pressure gradient given by

$$M_{F\infty} = \frac{f}{2D}\rho_f\langle j_f\rangle^2. \tag{4}$$

Here, f, D and j_f are, respectively, wall friction factor, channel diameter and superficial liquid velocity. The liquid velocity is approximately the same as the superficial liquid velocity in a single bubble system. Note that the second term on the right-hand-side of Eq. (3) is dropped when a single bubble is placed in a quiescent fluid.

For a dispersed two-phase flow, the averaged interfacial drag term, $\langle M_{ig}\rangle$, can be given approximately by Ishii and Mishima (1984)

$$\langle M_{ig}\rangle = -\frac{3}{8}\frac{C_D\rho_f}{\langle r_b\rangle}\langle\alpha_g\rangle\langle v_r\rangle|\langle v_r\rangle|, \tag{5}$$

where C_D and v_r are, respectively, drag coefficient for a multi-particle system and relative velocity between gas and liquid phases. Under steady-state condition without phase change and with negligible transverse pressure gradient and axial stress terms and the assumption that the averaged pressure and stress in the bulk fluid and at the interface are approximately the same, one-dimensional momentum equation for phase k can be simplified as (Ishii and Mishima, 1984; Hibiki and Ishii, 2003)

$$0 = -\langle\alpha_k\rangle\frac{\partial}{\partial z}\langle\langle p_m\rangle\rangle - \frac{4\alpha_{kw}\tau_{kw}}{D} - \langle\alpha_k\rangle\rho_k g_z + \langle M_{ik}\rangle - \langle\nabla\alpha_k\cdot\tau_i\rangle, \tag{6}$$

where p_m, α_{kw}, τ_{kw} and τ_i are, respectively, mixture pressure, void fraction of k phase at a wall, wall shear stress of k phase and interfacial stress. Assuming $\alpha_{gw} \simeq 0$ and $\alpha_{fw} \simeq 1$ under no phase change condition, the axial pressure gradient is obtained from gas and liquid momentum equations and the momentum jump condition at the interface as

$$\frac{\partial}{\partial z}\langle\langle p_m\rangle\rangle = -\rho_m g_z - \frac{4\tau_{fw}}{D} = -\rho_m g_z - M_F, \tag{7}$$

where ρ_m is mixture density and M_F is two-phase frictional pressure gradient defined by

$$M_F \equiv \frac{4\tau_{fw}}{D} = \left(-\frac{dp}{dz}\right)_F. \tag{8}$$

The subscript F indicates the frictional pressure loss. For simplicity, considering a uniform void profile, we can derive the interfacial drag term from Eqs. (6) and (7) as

$$\langle M_{ig}\rangle = -\langle\alpha_g\rangle\{\Delta\rho g_z(1-\langle\alpha_g\rangle) + M_F\}. \tag{9}$$

Substituting Eq. (9) into Eq. (5) yields

$$\langle v_r\rangle|\langle v_r\rangle| = \frac{8}{3}\frac{\langle r_b\rangle}{C_D\rho_f}\{\Delta\rho g_z(1-\langle\alpha_g\rangle) + M_F\}. \tag{10}$$

From Eqs. (3) and (10), we obtain

$$\frac{C_{D\infty}}{C_D} \equiv \left(\frac{\langle v_r\rangle}{v_{r\infty}}\right)^2 \frac{\Delta\rho g_z + M_{F\infty}}{\Delta\rho g_z(1-\langle\alpha_g\rangle) + M_F}. \tag{11}$$

By knowing $C_{D\infty}/C_D$, we can derive the drift velocity, which is related to the relative velocity by $v_{gj} = (1-\alpha_g)v_r$, from Eq. (11). The drag coefficient is dependent on the particle shape regime such as viscous regime (undistorted-particle regime), distorted-particle regime, churn-turbulent-flow regime and slug-flow regime (Ishii, 1977). As will be discussed later, the bubble size in a mini channel is mostly categorized as the viscous regime. In what follows,

we will develop the constitutive equation of the drift velocity in the viscous regime.

First, we assume that $C_{D\infty}/C_D$ can be predicted by the same expression as the local constitutive relation, provided the local values of flow parameters are replaced by area-averaged values (Ishii, 1977). Then, we introduce the similarity hypothesis that in the viscous regime a complete similarity exists between $C_{D\infty}$ based on single-bubble Reynolds number, $N_{Re\infty}$, and C_D based on multi-particle Reynolds number, N_{Re}, so that C_D has exactly the same functional form in terms of N_{Re} as $C_{D\infty}$ in terms of $N_{Re\infty}$ (Ishii, 1977) given by

$$C_{D\infty} = \frac{24}{N_{Re\infty}}(1 + 0.1N_{Re\infty}^{0.75}). \tag{12}$$

Reynolds numbers are defined as

$$N_{Re\infty} \equiv \frac{2r_b\rho_f v_{r\infty}}{\mu_f} \quad \text{and} \quad N_{Re} \equiv \frac{2\langle r_b\rangle\rho_f\langle v_r\rangle}{\mu_m}. \tag{13}$$

where μ_f and μ_m are, respectively, liquid and mixture viscosities. Note that Reynolds numbers based on relative velocity and bubble diameter is often utilized to characterize the bubble shape regime (Clift et al., 1978) which strongly affects the drag force acting on the bubble. By considering the two asymptotic cases of $N_{Re} \to 0$ and $N_{Re} \to \infty$ and interpolating between them, we obtain from Eq. (11)

$$\frac{\langle v_r\rangle}{v_{r\infty}} \simeq \{f(\langle\alpha_g\rangle)\}^2 \frac{\mu_m}{\mu_f} \frac{1 + 0.1N_{Re\infty}^{0.75}}{1 + 0.1N_{Re\infty}^{0.75}\{f(\langle\alpha_g\rangle)\}^{6/7}}, \tag{14}$$

where

$$f(\langle\alpha_g\rangle) \equiv \left\{\frac{\Delta\rho g_z(1 - \langle\alpha_g\rangle) + M_F}{\Delta\rho g_z + M_{F\infty}}\right\}^{1/2}\left(\frac{\mu_f}{\mu_m}\right). \tag{15}$$

The viscosity ratio, μ_m/μ_f for the case of gas viscosity, μ_g, negligibly smaller than μ_f is approximated by (Ishii, 1977)

$$\frac{\mu_m}{\mu_f} = (1 - \langle\alpha_g\rangle)^{-1} \quad \text{for } \mu_g \ll \mu_f. \tag{16}$$

By introducing the non-dimensional parameters for the relative velocity and bubble radius by $v_{r\infty}^* \equiv |v_{r\infty}|[\rho_f^2/\{\mu_f(\Delta\rho g_z + M_{F\infty})\}]^{1/3}$ and $r_b^* \equiv r_b\{\rho_f(\Delta\rho g_z + M_{F\infty})/\mu_f^2\}^{1/3}$, the terminal velocity for the viscous regime can be approximated from Eqs. (3) and (12) as (Ishii, 1977)

$$v_{r\infty}^* \simeq \frac{4.86}{r_b^*}\{(1 + 0.08r_b^{*3})^{4/7} - 1\}. \tag{17}$$

Consequently, the drift velocity for the viscous regime can be obtained from Eqs. (14) and (17) as

$$\langle\langle v_{gj}\rangle\rangle = \frac{10.8\mu_f}{\rho_f r_b}\psi(r_b^*)^{4/3}(1 - \langle\alpha_g\rangle)\{f(\langle\alpha_g\rangle)\}^2\frac{\mu_m}{\mu_f} \times \frac{1 + \psi(r_b^*)}{1 + \psi(r_b^*)\{f(\langle\alpha_g\rangle)\}^{6/7}}, \tag{18}$$

where

$$\psi(r_b^*) = 0.55\{(1 + 0.08r_b^{*3})^{4/7} - 1\}^{3/4}, \quad \text{for the viscous regime.} \tag{19}$$

Note that $N_{Re\infty}$ in Eq. (14) has been replaced by the new function ψ using the identity $N_{Re\infty} = 2r_b^* v_{r\infty}^*$ and Eq. (17). Eq. (18) holds for

$$N_{\mu f} \leqslant 0.11\{1 + \psi(r_b^*)\}/\{\psi(r_b^*)\}^{8/3}. \tag{20}$$

The viscous number is defined by

$$N_{\mu f} \equiv \frac{\mu_f}{\left(\rho_f\sigma\sqrt{\frac{\sigma}{\Delta\rho g_z + M_{F\infty}}}\right)^{1/2}}, \tag{21}$$

where σ is the surface tension. Note that the viscous number measures the viscous force induced by an internal flow to the surface tension force (Sleicher, 1962). Eq. (20) can be easily derived from Eq. (12) and the drag coefficient for distorted-particle regime (Ishii, 1977). For atmospheric air–water flow, the boundary between viscous and distorted-particle regimes is estimated to be about 2 mm from Eq. (20).

The constitutive equation for the drift velocity in distorted-particle regime without considering the effect of frictional pressure loss on the drift velocity, which is widely used in a bubbly-flow analysis, is given by (Ishii, 1977)

$$\langle\langle v_{gj}\rangle\rangle = \sqrt{2}\left(\frac{\sigma\Delta\rho g_z}{\rho_f^2}\right)^{1/4}(1 - \langle\alpha_g\rangle)^{1.75}. \tag{22}$$

Note that Eq. (22) may not be applicable to a mini channel flow with the channel diameter smaller than 2 mm.

2.3. Modeling of distribution parameter in mini channel

Ishii (1977) developed a simple correlation for the distribution parameter in bubbly-flow regime. Ishii first considered a fully developed bubbly flow and assumed that the distribution parameter would depend on the density ratio, ρ_g/ρ_f, and on the liquid Reynolds number, N_{Re_f} defined by $\rho_f\langle j_f\rangle D_H/\mu_f$ where ρ_g and D_H are, respectively, gas density and channel hydraulic diameter. Note that the liquid Reynolds number is the ratio of inertia force to viscous force. As the density ratio approaches unity, the distribution parameter should become unity. Based on the limit and various experimental data in fully developed flows, the distribution parameter was given approximately by

$$C_0 = C_\infty(N_{Re_f}) - \{C_\infty(N_{Re_f}) - 1\}\sqrt{\frac{\rho_g}{\rho_f}}, \tag{23}$$

where C_∞ is the asymptotic value of C_0. Here, the density group scales the inertia effects of each phase in a transverse void distribution. Physically, Eq. (23) models that the decrease in density difference, namely relative velocity tends to make the void distribution more homogeneous. Since the lift force is proportional to the relative velocity, reduced relative velocity causes reduced lift force acting on bubbles (Ishii and Hibiki, 2005).

For a laminar flow, C_∞ is 2 (Ishii, 1977), but due to the large velocity gradient, C_0 is very sensitive to $\langle\alpha_g\rangle$ at low void fractions. Ishii (1977) first evaluated C_0 in turbulent bubbly flow to be 1.2 based on available data at the time which showed the core peaked void fraction distribution. Hibiki and Ishii (2002b) proposed C_0 correlation in turbulent bubbly flow by taking the wall peaking phenomena in void fraction distribution into account. In the correlation, C_0 is presented as a function of bubble diameter, which is a key parameter to determine the direction of the lift force. It is well-known that the lift force direction strongly depends on the bubble diameter. Zun (1988) reported that distinctive higher bubble concentration at the wall region if the bubble equivalent sphere diameter appeared in the range of 0.8 and 3.6 mm. He also pointed out that intermediate void fraction distributions occurred at bubble sizes either between 0.6 and 0.8 mm or 3.6 and 5.1 mm and that bubbles smaller than 0.6 mm or larger than 5.1 mm tended to concentrate at the channel center. Thus, for a turbulent flow in a mini channel, bubbles may be considered to migrate towards the channel center and C_∞ may be approximated to be 1.2. Taking account of the flow transition from a laminar flow to a turbulent flow, C_∞ in the bubbly-flow regime is approximated by

$$C_\infty = 2.0\exp(cN_{Re_f}) + 1.2\{1 - \exp(cN_{Re_f})\}. \tag{24}$$

The coefficient, c, is approximately estimated to be -0.000584 by the condition of $\exp(cN_{Re_f}) = 0.5$ at $Re_f = 1189$, which corresponds to the Reynolds number at the intersection point of laminar friction factor with turbulent friction factor. Thus,

$$C_\infty = 2.0\exp(-0.000584N_{Re_f}) + 1.2\{1 - \exp(-0.000584N_{Re_f})\}. \tag{25}$$

The constitutive equation for the distribution parameter in the bubbly-flow regime is given by

$$C_0 = \left\{2.0e^{-0.000584N_{Re_f}} + 1.2(1 - e^{-0.000584N_{Re_f}})\right\} - \left[\left\{2.0e^{-0.000584N_{Re_f}} + 1.2(1 - e^{-0.000584N_{Re_f}})\right\} - 1\right]\sqrt{\frac{\rho_g}{\rho_f}}. \tag{26}$$

For large N_{Re_f}, Eq. (26) is simplified to Ishii's equation (Ishii, 1977) for the turbulent bubbly-flow regime in a round pipe as

$$C_0 = 1.2 - 0.2\sqrt{\frac{\rho_g}{\rho_f}}. \tag{27}$$

2.4. Interfacial area concentration model

Recently, we successfully developed the model of interfacial area concentration, a_i, or bubble Sauter mean diameter, D_{Sm}, under steady fully-developed bubbly flows based on rigorous interfacial area transport equation with modeled sink and source terms for the interfacial area concentration (Hibiki and Ishii, 2001, 2002a; Hibiki et al., 2006). The inverse of the interfacial area concentration is one of the important length scales in two-phase flow. In the model, the interface structure length scale is expressed as a function of space probability such as void fraction, system length scale such as hydraulic equivalent diameter of a flow channel, internal length scale such as Laplace length, $Lo(\equiv\sqrt{\sigma/(\Delta\rho g_z)})$, and a parameter characterizing turbulence in a flow. Note that Laplace length scale measures the critical wavelength of the Taylor instability which is also the maximum stable drop radius in the free stream. The Laplace length is often utilized to estimate the bubble diameter in some nuclear thermal-hydraulic system analysis codes. The applicability of the interfacial area concentration model up to 9 mm pipe has been confirmed (Hibiki and Ishii, 2002a). Thus, it may be reasonable to evaluate the applicability of the interfacial area concentration model to mini channel flow. In what follows, the interfacial area concentration model is briefly explained.

The interfacial area concentration model is expressed by (Hibiki and Ishii, 2002a)

$$N_{a_i} = 3.02N_{Lo}^{0.335}\alpha_g N_{Re_b}^{0.239} \quad \text{or} \quad N_{D_{Sm}} = 1.99N_{Lo}^{-0.335}N_{Re_b}^{-0.239}. \tag{28}$$

Non-dimensional interfacial area concentration, bubble Sauter mean diameter and Laplace length and bubble Reynolds number are defined by

$$N_{a_i} \equiv \langle a_i\rangle Lo, \quad N_{D_{Sm}} \equiv \frac{\langle D_{Sm}\rangle}{Lo}, \quad N_{Lo} \equiv \frac{Lo}{D_H} \quad \text{and} \quad N_{Re_b} \equiv \frac{\langle\varepsilon\rangle^{1/3}Lo^{4/3}}{\nu_f}, \tag{29}$$

where ν_f is kinematic viscosity. Note that non-dimensional interfacial area concentration measures void fraction and non-dimensional bubble Sauter mean diameter measures the difference between the bubble size and the maximum stable bubble size. Non-dimensional Laplace length represents the bubble size relative to the system length scale and bubble Reynolds number defined based on the turbulent velocity and Laplace length characterizes the driving potential for bubble coalescence and breakup.

An expression for the energy dissipation rate per unit mass can be obtained from the mechanical energy balance on the assumption that the dissipation of turbulent energy in the flow is equal to its productions as (Hibiki and Ishii, 2002a)

$$\langle\varepsilon\rangle = g_z|\langle j_g\rangle|\exp(-0.000584N_{Re_f}) + \frac{|\langle j\rangle|}{\rho_m}\left(-\frac{dp}{dz}\right)_F\{1 - \exp(-0.000584N_{Re_f})\}. \tag{30}$$

The first and second terms on the right-hand-side of Eq. (30) are due to bubble expansion and wall friction, respectively.

The interfacial area concentration model, Eq. (28), was validated by 494 adiabatic flow data sets measured in

bubble columns and forced convective bubbly flows (Hibiki and Ishii, 2002a; Hibiki et al., 2003, 2004). These data sets covered extensive loop and flow conditions such as flow type (bubble column or forced convective bubbly flow), channel geometry (circular, rectangular or annulus channel), channel hydraulic equivalent diameter (9.0 mm $\leqslant D_H \leqslant$ 5500 mm), flow direction (vertical upward, horizontal or vertical downward flow), superficial gas velocity (0.000788 m/s $\leqslant \langle j_g \rangle \leqslant$ 4.87 m/s), superficial liquid velocity (0.00 m/s $\leqslant \langle j_f \rangle \leqslant$ 6.55 m/s), liquid density (684 kg/m^3 $\leqslant \rho_f \leqslant$ 1594 kg/m^3), liquid viscosity (0.410 mPa s $\leqslant \mu_f \leqslant$ 21.1 mPa s), and surface tension (20.0 m N/m $\leqslant \sigma \leqslant$ 75.0 m N/m). An excellent agreement was obtained between the interfacial area concentration model and 494 adiabatic flow data within the averaged relative deviation of 21.6%. Additional comparison with 110 developing flow data confirmed the validity of Eq. (28) at $z/D \geqslant 10$ in the tested channels if about 30% prediction error is accepted. However, it is anticipated that longer distance may be required for mini channels since enough bubble contact time is needed to make flows fully-developed.

3. Experiments

Fig. 1 shows the schematic diagram of a flow loop. In this experiment, the non-intrusive image processing method was utilized to measure axial developments of flow parameters. The test section was a round pipe made of a fluorinated ethylene propylene pipe with the reflex index of 1.34 similar to that of water (=1.33) to avoid the image distortion. The inner diameter was determined by using the analytical solution of the friction factor for laminar flow as follows (Mishima and Hibiki, 1996). The friction factor for the laminar flow in a round pipe is given by the following well-known equation for Hagen–Poiseuille flow as

$$f = \frac{64}{N_{Re_f}}. \tag{31}$$

The inner diameter was determined from the above equation by using the measured friction factor, measured flow velocity and the fluid properties, see Fig. 2. The error of the diameter so obtained was estimated to be within ±1%. The inner diameter, D, and length, L, of the pipe were 1.02 mm and 500 mm, respectively, and the L/D of the test section was 490.

Nitrogen gas was supplied from a nitrogen bottle and was introduced into a mixing chamber through a gas injector. As shown in Fig. 3, the gas injector consisted of a bubble injection nozzle with the inner and outer diameters of 0.1 and 0.3 mm, respectively, and tapered acrylic cylinder. No significant swirl flow near the test section inlet was observed based on video images of the trajectories of dispersed bubbles. The nitrogen gas and purified water with the electrical conductivity lower than 1 μS/cm were mixed in the mixing chamber and the mixture flowed through

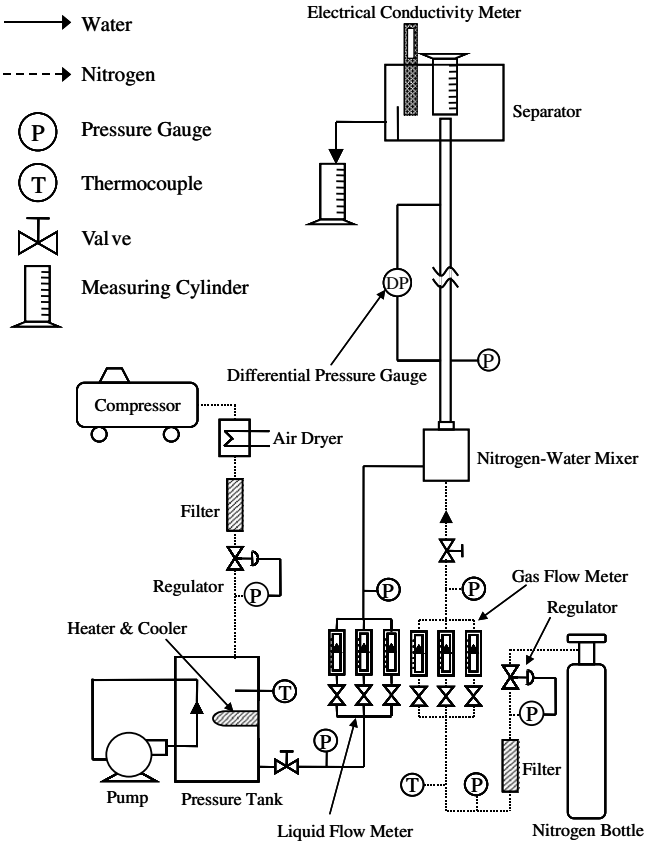

Fig. 1. Schematic diagram of flow loop.

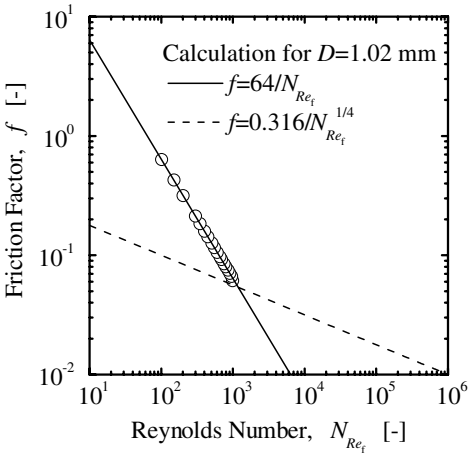

Fig. 2. Single-phase friction factor.

the test section. After flowing through the test section, the nitrogen gas and water were collected to measure their volumes. As shown in Fig. 1, the nitrogen gas was collected by a measuring cylinder placed in the gas–liquid separator, and the collected volume per unit time was measured. The overflow water from the gas–liquid separator was also collected by a measuring cylinder, and the collected volume per unit time was measured. Thus, the gas and liquid flow rate were

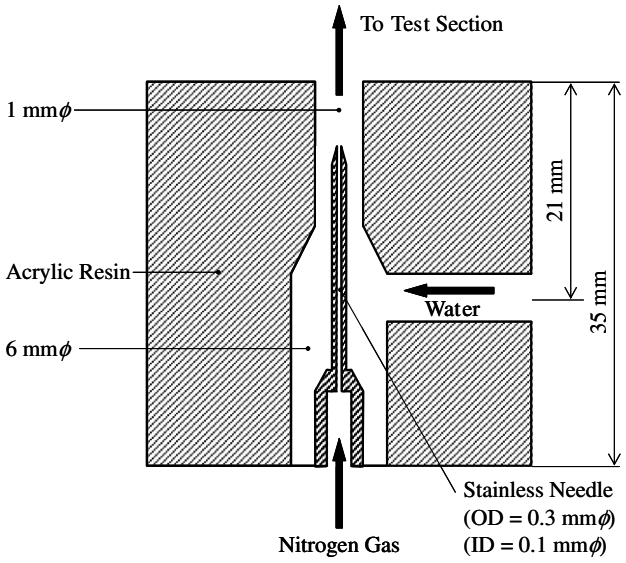

Fig. 3. Schematic diagram of mixing chamber.

determined by the collected gas and liquid volumes, respectively. The gas and liquid flow rate measured by the measuring cylinder agreed with those measured by gas and liquid flow meters installed at the upstream of the test section inlet within ±10%. It should be noted here that saturated solubility of nitrogen to water is negligible in the tested experimental conditions. The loop temperature was kept at a room temperature (20 °C) within ±0.5 °C. The difference between the inlet and outlet temperatures was within ±0.5 °C, and thus the temperature drop due to the gas expansion along the test section could be negligible. The pressure and differential pressure measurements were conducted by a pressure sensor and differential pressure cell, respectively. The pressure devices detected the system pressure and differential pressure through a tiny hole with a diameter of 0.2 mm created on the test section wall. The pressure measurements were performed at the downstream of 100 mm ($z/D = 98.0$) and 410 mm ($z/D = 402$) from the mixing chamber. Because the locations of the pressure tap were away from the test section inlet and outlet, the pressure disturbance due to the inlet and outlet was not considered. The measurement accuracy is estimated to be ±1% for conservative estimate. The electric conductivity meter was installed at the gas–liquid separator to monitor the water quality. The experiment was performed at the electric conductivity smaller than 1 μS.

The flow measurements were performed by the image processing method with a digital video camera and a stroboscope with the flashing time of 0.3 μs at $z/D = 15.0$, 75.0, 150, 250, and 450. The water boxes were placed at the measuring stations to minimize the image distortion due to the inflection. Bubble images taken by the digital video camera were transmitted to a personal computer equipped with an image-processing board. The image-processing to obtain dimensions of bubbles was performed by the following procedure.

1. Reading and bordering the images.
2. Image enhancement and data smoothing for noise reduction.
3. Median-filtering the images at eight-neighbor pixels of a specific pixel.
4. Binarization of the pixels to extract the outer boundaries of the bubbles.
5. Labeling the bubbles.
6. Measuring bubble dimensions such as major and minor axes.

The void fraction, interfacial area concentration, and bubble Sauter mean diameter were calculated from the obtained images with an assumption of an axisymmetric bubble, and the bubble number density defined as the total number of bubbles per unit volume was simply determined by counting the number of bubbles.

Typical bubble images are shown in Fig. 4. As can be seen in Fig. 4, the bubble shape appeared to deviate from an axisymmetric bubble in some degree. However, as will be described later, measured flow parameters agreed with those measured by other reference methods within ±15% by conservative estimate. Thus, the assumption of an axisymmetric bubble was acceptable within the measurement error of ±15%. The methodology of the image-processing method was detailed in our previous papers (Takamasa et al., 2003). Fig. 5 shows the relationship between the relative deviation from averaged void fraction, E, defined by Eq. (32) and the number of processed images.

$$E \equiv \frac{\left|\langle \alpha_g \rangle_N - \langle \alpha_g \rangle_{1000}\right|}{\langle \alpha_g \rangle_{1000}} \times 100, \tag{32}$$

where $\langle \alpha_g \rangle_N$ and $\langle \alpha_g \rangle_{1000}$ are void fractions obtained by processing N images and 1000 images, respectively. This figure clearly shows that the measured void fraction converges on a certain void fraction within ±3% at the number of processed images higher than 50. About 3000–4000 bubbles were sampled to maintain similar statistics between the different combinations of experimental conditions. The void fractions measured by the image-processing method agreed with those obtained in a 1.09-mm round pipe by neutron radiography (Mishima and Hibiki, 1996) within the averaged relative deviation of 12.3%. The image-processing method for the interfacial area concentration measurement was also validated by a double-sensor conductivity probe method. The separate test was performed in a 25.4-mm round pipe and a good agreement in the interfacial area concentration measurement was obtained between them within the averaged relative deviation of 6.95% (Hibiki et al., 1998). Since the measurement accuracy of the double sensor probe method is reported to be ±7% (Wu and Ishii, 1999), the measurement accuracy of the image processing method is within ±15% by conservative estimate. The experimental conditions are tabulated in Table 1.

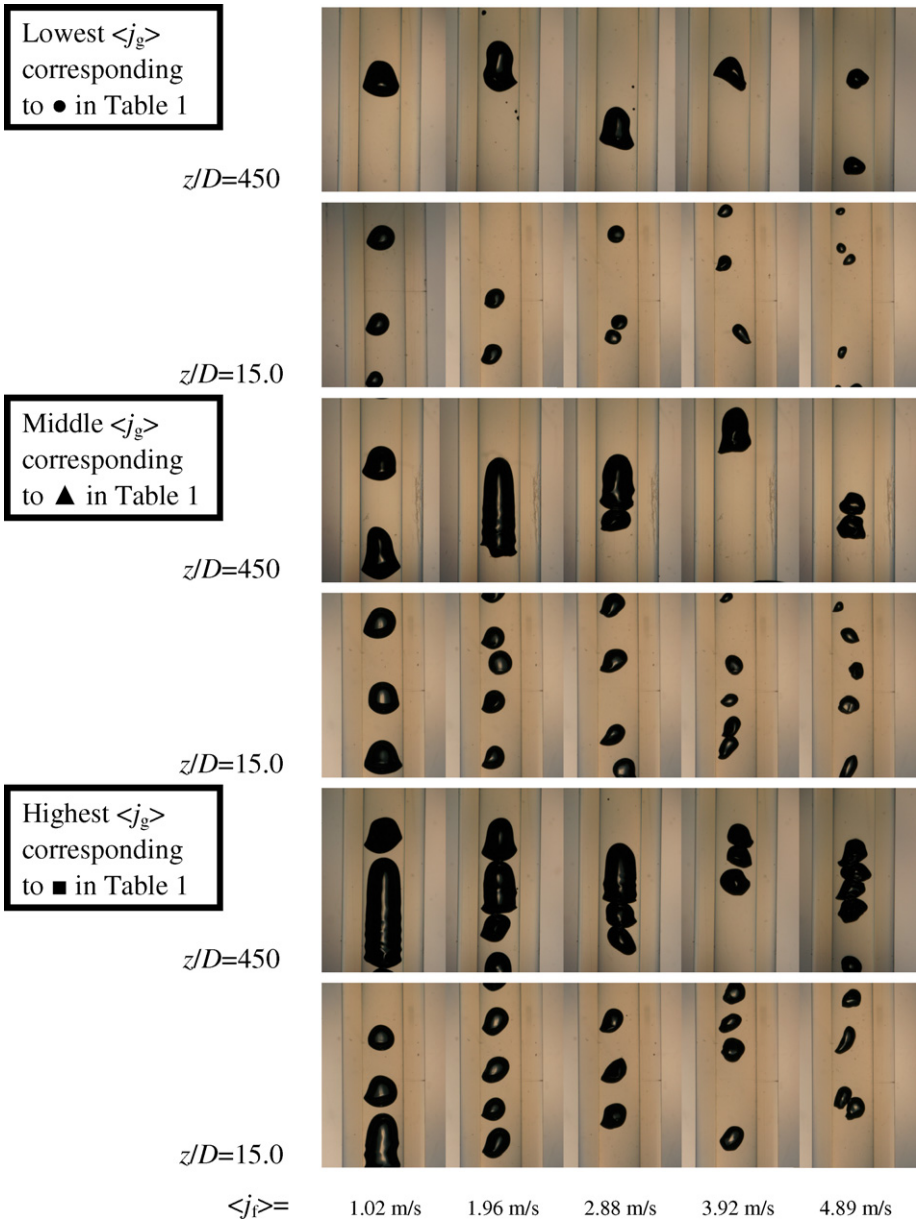

Fig. 4. Typical bubble images.

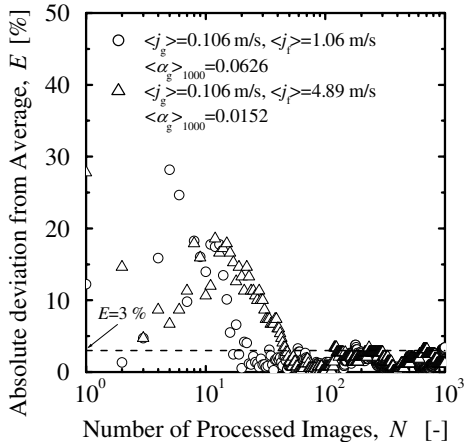

Fig. 5. Effect of number of processed images on measured void fraction.

4. Results and discussion

4.1. Void fraction

Fig. 6 shows the axial developments of void fraction. The first, second, third, fourth, and fifth figures from the left indicate the data taken at $\langle j_f \rangle = 1.02$, 1.96, 2.88, 3.92, and 4.89 m/s, respectively. The experimental conditions for each symbol and line are shown in Table 1. The error bar indicates the measurement error of ±15%. The lines indicate the values calculated by the drift-flux model, Eq. (1), with the distribution parameter given by Eq. (26) and the drift velocity given by Eq. (18). In Eq. (18), the frictional pressure loss gradient of liquid single-phase flow, $M_{F\infty}$, is calculated by Eq. (4) with the friction factors for

Table 1
Flow conditions in this experiment[a]

Symbols and lines	• —	▲ ---	■ ···
$\langle j_f \rangle$ [m/s]	$\langle j_g \rangle_{z/D=15.0}$ [m/s]	$\langle j_g \rangle_{z/D=15.0}$ [m/s]	$\langle j_g \rangle_{z/D=15.0}$ [m/s]
1.02	0.0959 (5.00)	0.292 (13.3)	0.472 (19.5)
1.96	0.0877 (2.85)	0.283 (7.31)	0.447 (11.1)
2.88	0.0817 (1.81)	0.229 (5.07)	0.428 (8.83)
3.92	0.0741 (1.17)	0.236 (3.88)	0.398 (5.81)
4.89	0.0754 (0.982)	0.232 (2.74)	0.392 (5.03)

[a] Values in the parentheses indicate the void fractions in % measured at $z/D = 15.0$.

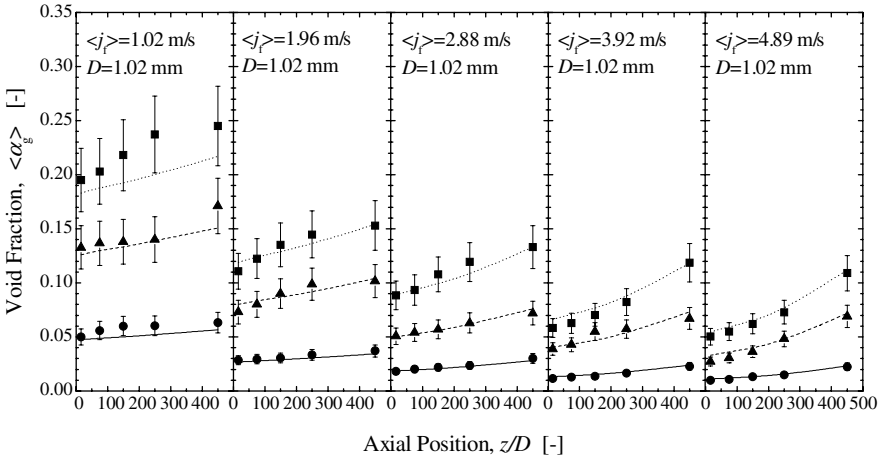

Fig. 6. Axial development of void fraction.

laminar and turbulent flows given by Eqs. (31) and (33), respectively.

$$f = \frac{0.316}{N_{Re_f}^{1/4}}. \tag{33}$$

The friction pressure loss gradient of two-phase flow, M_F, can be calculated by Lockhart–Martinelli's method (Lockhart and Martinelli, 1949) with Chisholm's equation given by Eq. (34) (Chisholm, 1967) and Chisholm's parameter, C, given by Eq. (35) (Mishima and Hibiki, 1996).

$$\Phi_f^2 = 1 + \frac{C}{X} + \frac{1}{X^2}, \tag{34}$$

$$C = 21(1 - e^{-0.333D}). \tag{35}$$

The two-phase friction multiplier, Φ_f^2, and Martinelli parameter, X are defined as

$$\Phi_f^2 \equiv \frac{(dp/dz)_F}{(dp/dz)_{f\text{-}1\phi}} \quad \text{and} \quad X^2 \equiv \frac{(dp/dz)_{f\text{-}1\phi}}{(dp/dz)_{g\text{-}1\phi}}, \tag{36}$$

where the subscripts of f-1ϕ and g-1ϕ are the frictional pressure loss when either the liquid or the gas component flows in the pipe as a single-phase flow, respectively. In Eq. (35), the unit of D should be in mm. Eq. (35) was validated in mini channels with the pipe diameter ranging from 1 to 4 mm (Mishima and Hibiki, 1996). As shown in Fig. 7, Eq. (34) with Eq. (35) agrees with the data in

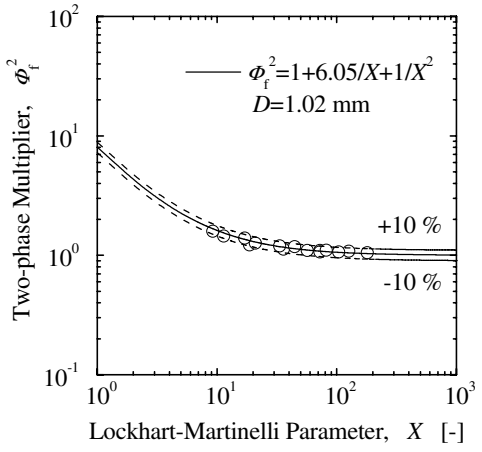

Fig. 7. Lockhart–Martinelli correlation for frictional pressure loss.

the present experiment with the averaged relative deviation of 2.14%. The friction pressure loss gradient of two-phase flow is expressed as a function of the void fraction for given superficial gas and liquid velocities. Thus, the void fraction for given superficial gas and liquid velocities can be determined from Eqs. (1), (18), and (26) numerically.

As shown in Fig. 6, significant increase of the void fraction along the flow direction is observed in the tested experimental conditions. This is mainly attributed to the pressure reduction along the flow direction. A good agreement

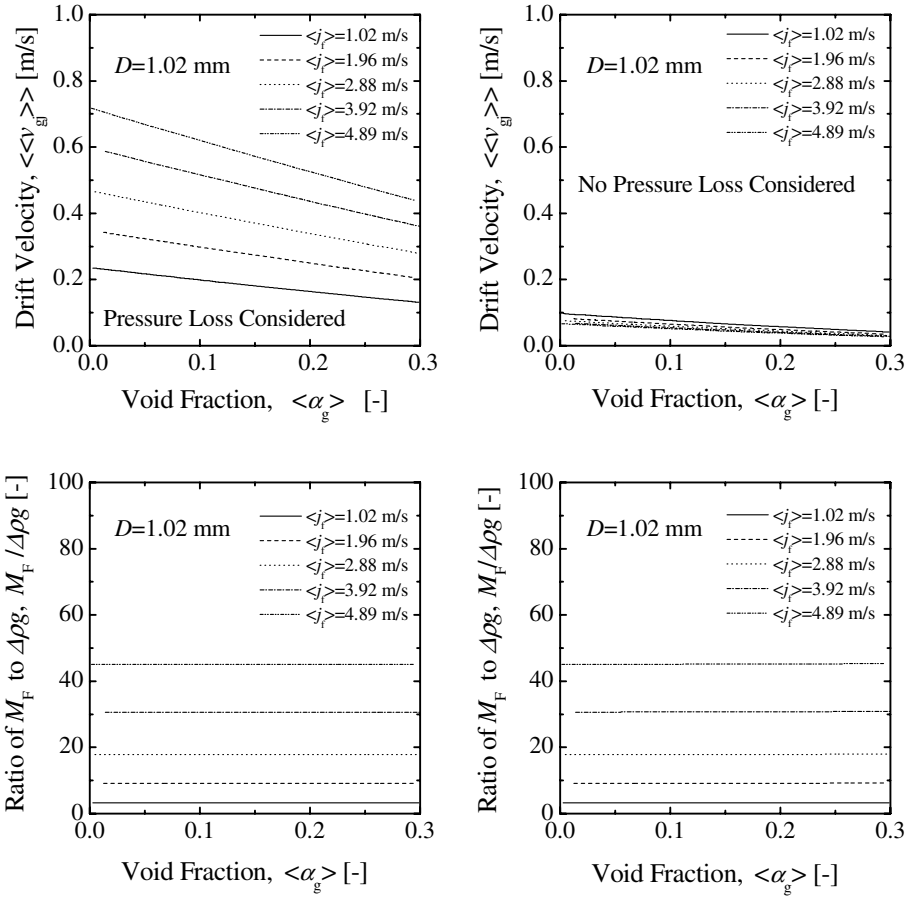

Fig. 8. Effect of the pressure loss on the drift velocity and the ratio of the frictional pressure loss to the gravitational pressure loss.

between the drift-flux model and the data is obtained within the averaged relative deviation of 6.76%, and the drift-flux model reproduces the tendency of the axial development of the void fraction very well.

Fig. 8 shows the effect of the pressure loss on the drift velocity and the ratio of the frictional pressure loss to the gravitational pressure loss. It should be noted here that the accelerational pressure loss is negligibly small in the tested experimental conditions. It can be seen from the lower figures that the frictional pressure loss dominates the pressure loss in the tested flow conditions. As can be seen from the upper right figure, the drift velocities calculated by Eq. (18) neglecting the frictional pressure loss terms indicate that the drift velocities are lower than 0.1 m/s in the tested experimental conditions. The drift velocities calculated by Eq. (18) considering the frictional pressure loss are shown in the upper left figure. The upper left figure indicates that the drift velocity is enhanced by increasing the superficial liquid velocity or the frictional pressure loss.

4.2. Interfacial area concentration

Fig. 9 shows the axial developments of interfacial area concentration. The first, second, third, fourth, and fifth figures from the left indicate the data taken at $\langle j_f \rangle = 1.02$, 1.96, 2.88, 3.92, and 4.89 m/s, respectively. The experimental conditions for each symbol and line are shown in Table 1. The error bar indicates the measurement error of ±15%. The lines indicate the values calculated by the interfacial area concentration model, Eq. (28).

As shown in the figure, the interfacial area concentration tends to increase along the flow direction in the tested experimental conditions. Since the bubble number density decreases along the flow direction as shown in Fig. 10, the axial increase of the interfacial area concentration is mainly attributed to the pressure reduction along the flow direction. A fairly good agreement between the model and the obtained data including Taylor bubble data is obtained within the averaged relative deviation of 17.5%, and the model reproduces the tendency of the axial development of the interfacial area concentration very well.

However, the deviation between the calculated and measured values is observed in some flow conditions where some Taylor bubbles are formed, see the data indicated by dotted circles in Fig. 9. Since Eq. (28) is only applicable to bubbly flow regime where no cap and Taylor bubble is formed, the prediction accuracy is deteriorated in such flow conditions. As shown in Fig. 11, in most of flow conditions the bubble diameters are larger than the

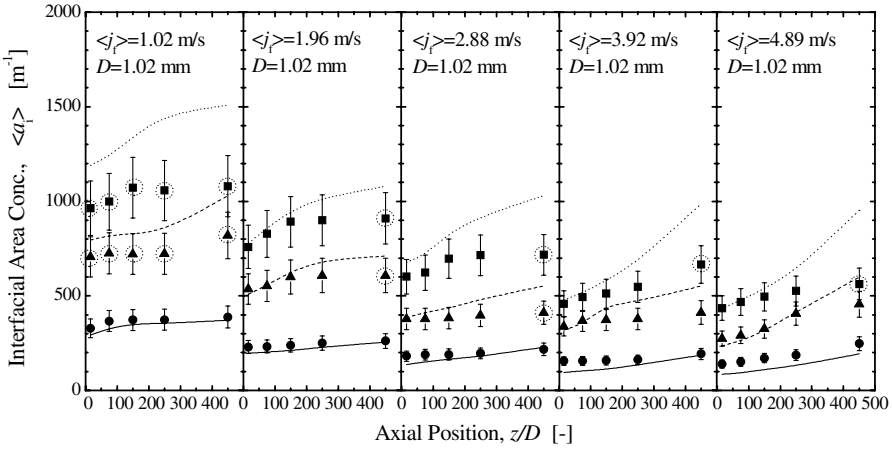

Fig. 9. Axial development of interfacial area concentration.

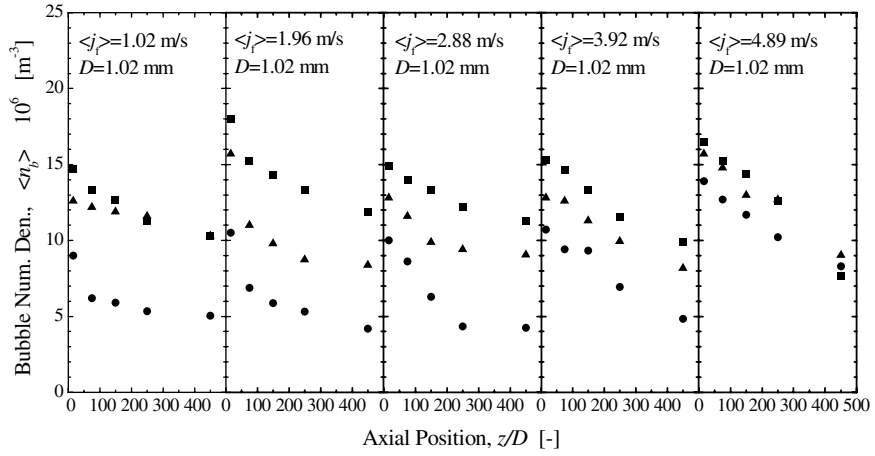

Fig. 10. Axial development of bubble number density.

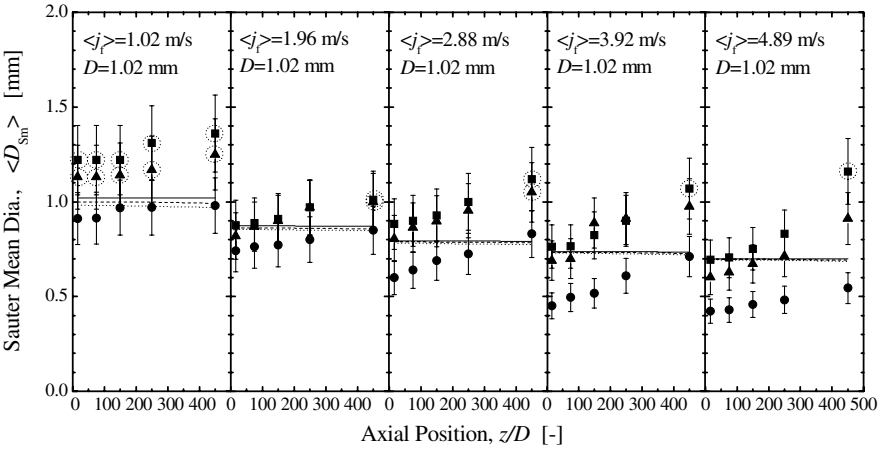

Fig. 11. Axial development of bubble Sauter mean diameter.

pipe diameter at $z/D = 450$. Thus, in most of flow conditions, the predicted interfacial area concentrations overestimate the measured interfacial area concentrations at $z/D = 450$.

4.3. Gas velocity

Fig. 12 shows the axial developments of gas velocity. The first, second, third, fourth, and fifth figures from the

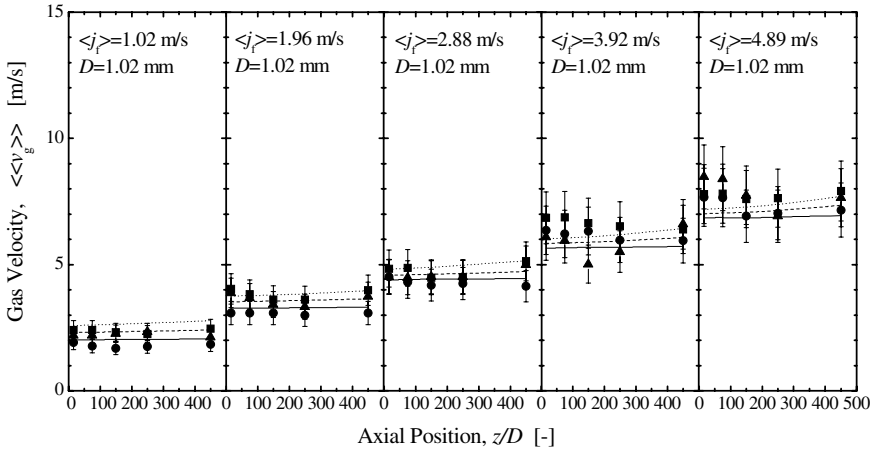

Fig. 12. Axial development of gas velocity.

left indicate the data taken at $\langle j_f \rangle = 1.02$, 1.96, 2.88, 3.92, and 4.89 m/s, respectively. The experimental conditions for each symbol and line are shown in Table 1. The error bar indicates the measurement error of ±15%. The lines indicate the values calculated by the drift-flux model with Eqs. (18) and (26).

As shown in the figure, insignificant change of the gas velocity along the flow direction is observed in the tested experimental conditions except for $\langle j_f \rangle = 3.92$ and 4.89 m/s. In this experiment, due to the converging section in the mixing chamber, the bubbles tended to be converged in the channel center near the test section inlet resulting in higher gas velocity, and as the flow developed, the bubbles were redistributed over the flow channel resulting in lower gas velocity. The insignificant axial change of the gas velocity for relatively low liquid velocity indicates the insignificant changes of the void and velocity distributions along the axial direction. This means that in such flow conditions relatively rapid redistribution of bubbles injected at the test section inlet over the flow channel occurs within a short distance from the test section inlet. On the contrary, the flow in relatively high liquid velocity requires much longer axial length to redistribute bubbles injected at the test section inlet over the flow channel. For $\langle j_f \rangle = 3.92$ and 4.89 m/s, the flow seems to become fully developed at the distance of $z/D \approx 100$.

A good agreement between the drift-flux model and the data is obtained within the averaged relative deviation of 6.84%, and the drift-flux model reproduces the tendency of the axial development of the gas velocity except for the flows near the test section inlet at $\langle j_f \rangle = 3.92$ and 4.89 m/s very well. Fig. 13 shows the comparison of the data with various drift-flux models. The solid lines indicate the predictions by the drift-flux model with Eqs. (18) and (26). Just for reference, the prediction results by the drift-flux model with Eqs. (22) and (27) at $\langle \alpha_g \rangle = 0$ and $\langle \alpha_g \rangle = 0.3$ are also indicated by the broken and dotted lines, respectively. The drift-flux model developed for conventional pipes without considering frictional pressure loss, Eqs. (22) and (27) tends to underestimate the gas velocity in a mini channel. This is mainly attributed to the difference in the drift-velocity between Eqs. (18) and (22). The difference in the predicted gas velocities between two models at $\langle j \rangle$ = 5-to-6 m/s is about 0.7 m/s, which corresponds to the difference in the predicted drift velocity, see Fig. 8, since the distribution parameters predicted by Eqs. (26) and (27) are almost the same, namely 1.2.

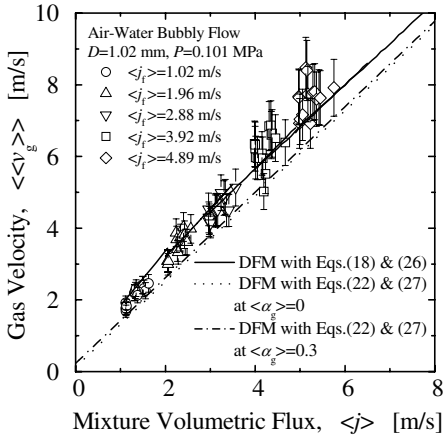

Fig. 13. Drift-flux plot of the gas velocity.

4.4. Bubble Sauter mean diameter

Fig. 11 shows the axial developments of bubble Sauter mean diameter. The first, second, third, fourth, and fifth figures from the left indicate the data taken at $\langle j_f \rangle = 1.02$, 1.96, 2.88, 3.92, and 4.89 m/s, respectively. The experimental conditions for each symbol and line are shown in Table 1. The error bar indicates the measurement error of ±15%. The lines indicate the values calculated by the model of the bubble Sauter mean diameter, Eq. (28).

As shown in the figure, the bubble Sauter mean diameter tends to increase along the flow direction in the tested experimental conditions. Since the bubble number density decreases along the flow direction as shown in Fig. 10, the axial increase of the bubble Sauter mean diameter is

mainly attributed to the pressure reduction along the flow direction, see Fig. 6 and the bubble coalescence, see Figs. 4 and 10. For example, about 30% increase of the bubble diameter is expected by the measured pressure reduction between $z/D = 15$ and 450 for the flow condition such as $\langle j_g \rangle_{z/D=15.0} = 0.392$ m/s and $\langle j_f \rangle = 4.89$ m/s. A fairly good agreement between the model and the obtained data including Taylor bubble data is obtained within the averaged relative deviation of 17.4%. The prediction error in the bubble Sauter mean diameter is similar to that in the interfacial area concentration, since the relation such as $D_{Sm} = 6\alpha/a_i$ exists among bubble Sauter mean diameter, interfacial area concentration, and void fraction. Although the averaged relative deviation of 17.4% indicates the validity of the model, it is clearly seen from Fig. 11 that the predicted bubble Sauter mean diameters disagree with the measured ones at relatively small z/D. The model was validated under steady fully-developed condition and developing flow at $z/D \geqslant 10$ in common pipes with the diameter larger than 9 mm. In mini pipes, the longer distance may be necessary to make the flow fully-developed since enough bubble contact time is required. Thus, the disagreement between the predicted and measured bubble Sauter mean diameters at relatively small z/D may be attributed to insufficient developing length.

The deviation between the calculated and measured values is observed in some flow conditions where some Taylor bubbles are formed, see the data indicated by dotted circles in Fig. 11. Since the model is applicable to bubbly flow regime, the prediction accuracy is deteriorated in such flow conditions. Thus, in the flow conditions where the bubble Sauter mean diameter is larger than the pipe diameter (=1.02 mm), the predicted Sauter mean diameters underestimate the measured Sauter mean diameter.

4.5. Bubble number density

Fig. 10 shows the axial developments of bubble number density. The first, second, third, fourth, and fifth figures from the left indicate the data taken at $\langle j_f \rangle = 1.02$, 1.96, 2.88, 3.92, and 4.89 m/s, respectively. The experimental conditions for each symbol are shown in Table 1. As shown in the figure, the bubble number density tends to decrease along the flow direction in the tested experimental conditions due to the bubble coalescence.

In order to emphasize the degree of the bubble breakup and coalescence between two measuring sections, the following bubble breakup and coalescence index, ξ, is introduced here

$$\xi \equiv \frac{\langle n_b^d \rangle - \langle n_b^u \rangle}{(\langle n_b^d \rangle + \langle n_b^u \rangle)/2}, \tag{37}$$

where the superscripts of d and u are the data measured at downstream and upstream, respectively. The numerator and denominator indicates the change of the bubble number density between two measuring sections and the averaged bubble number density between two measuring sections, respectively. Thus, the bubble breakup and coalescence index shows the dominant bubble interaction mechanism between two measuring sections and its degree. The positive and negative indexes mean the dominant mechanisms to be bubble breakup and coalescence, respectively. It should be noted here that the increase in the bubble Sauter mean diameter is approximately in proportional to third root of the decrease in the bubble number density, namely $(\langle n_b^u \rangle / \langle n_b^d \rangle)^{1/3}$. This means that the decrease in the bubble number density causes the insignificant increase in the bubble Sauter mean diameter. For example, 25% decrease of the bubble number density causes 10% increase in the bubble Sauter mean diameter.

Fig. 14 shows the axial change of the bubble breakup and coalescence index. The following approximate tendencies can be found from the figure as

(i) For $\langle j_f \rangle = 1.02$ m/s and $\langle \alpha_g \rangle_{z/D=15.0} = 5.00\%$, the initial bubble size may be small to be in its equilibrium of bubble coalescence and breakup (Hibiki and Ishii, 2002c), and then intensive bubble coalescence occurs

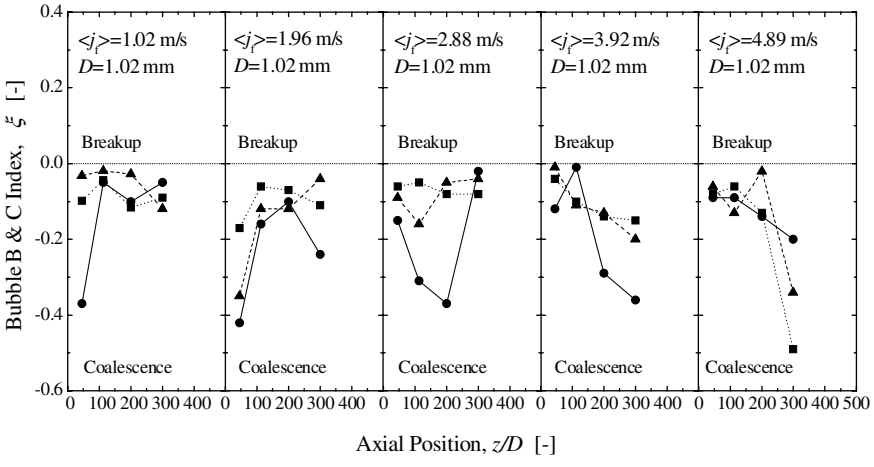

Fig. 14. Axial change of bubble breakup and coalescence index.

near the test section inlet. Such intensive bubble coalescence appears to terminate up to $z/D = 75$, resulting in insignificant axial change of the bubble breakup and coalescence index at the downstream of $z/D = 75$. As can be seen from Fig. 11, the bubble size reaches the channel diameter at the test section outlet, which means that Taylor bubbles are formed at the test section outlet, see Fig. 4. As the void fraction increases, intensive bubble coalescence occurs near the test section inlet, and appears to terminate even at the first measuring section at $z/D = 15$. For $\langle j_f \rangle = 1.96$ and 2.88 m/s, the similar tendency is also observed.

(ii) For higher liquid velocities such as $\langle j_f \rangle = 3.92$ and 4.89 m/s, the initial bubble size may be small to be in its equilibrium of bubble coalescence and breakup (Hibiki and Ishii, 2002c), and then the bubble coalescence is enhanced along the flow direction. Since sufficient bubble contact time may be needed to complete the bubble coalescence (Oolman and Blanch, 1986), the bubble breakup and coalescence index tends to decreases along the flow direction for higher liquid velocities.

Thus, the bubble interaction mechanism appears to be very complicated. In order to predict such complicated transport phenomena, the interfacial area transport equation is promising (Hibiki and Ishii, 2002c, 2000a,b). Although the present study proposed two mechanistic models to predict void fraction and interfacial area concentration and offered the database of extensive developing flow parameters in the mini channel with 1.02-mm inner diameter, more rigorous and extensive data in mini channels will be indispensable to develop and evaluate the reliable models to predict various flow parameters, particularly, interfacial area concentration.

5. Conclusions

In relation to the cooling of a diverter of a fusion reactor, high power electronic devices and compact heat exchangers, it has become important to understand the characteristics of gas–liquid two-phase flow in a mini channel. Accurate prediction of the flow parameters is essential to successful development of the interfacial transfer terms in the two-phase flow formulation. Mechanistic modeling of the interfacial transfer terms entirely relies on accurate local flow measurements over extensive flow conditions and channel geometries. From this point of view, the drift-flux model development and the evaluation of the interfacial area concentration model were conducted and axial measurements of flow parameters such as void fraction, interfacial area concentration, gas velocity, bubble Sauter mean diameter, and bubble number density were performed by the image-processing method in vertical upward bubbly flows using a 1.02 mm-diameter pipe. The measurements were performed at five axial locations of $z/D = 15.0$, 75.0, 150, 250 and 450. A total of 15 data sets were acquired consisting of 75 (=15 flow conditions × 5 axial locations) data points. The flow conditions cover the void fractions from 0.980% to 24.6% and the superficial liquid velocities from 1.02 m/s to 4.89 m/s. The obtained results are summarized as follows:

(1) The constitutive equation for the drift velocity applicable to mini channel flow was developed by considering the effect of the frictional pressure loss on the drift velocity. The constitutive equation for the distribution parameter was also developed by considering the flow transition from laminar to turbulent flows. The drift-flux model with the modeled constitutive equations for the distribution parameter and drift velocity was compared with the measured data. It reproduced the axial developments of the void fraction and gas velocity very well. The averaged prediction accuracies of one-dimensional void fraction and gas velocity were estimated to be within ±6.76% and ±6.84%, respectively.

(2) The applicability of the interfacial area concentration model, Eq. (28), to mini channel flow was examined by the measured data. It reproduced the axial developments of the interfacial area concentration very well at the flow conditions where no Taylor bubble was formed. However, once Taylor bubbles were formed, the model tended to overestimate the interfacial area concentration significantly. Thus, the development of the interfacial area transport equation was recommended to predict such interfacial area transport process accurately. Overall averaged relative deviation between the model and the data was within 17.5%.

(3) The dominant bubble interaction mechanism was displayed by the newly defined bubble breakup and coalescence index. The dominant bubble interaction mechanism turned out to be bubble coalescence in the tested conditions.

Acknowledgement

The authors are very thankful to Messrs. Y. Fukuhara, N. Fukamachi and N. Tamura of Tokyo University of Marine Science and Technology for their assistance in the experiment.

References

Chisholm, D., 1967. A theoretical basis for the Lockhart–Martinelli correlation for two-phase flow. Int. J. Heat Mass Transfer 10, 1767–1778.

Clift, R., Grace, J.R., Weber, M.E., 1978. Bubbles, Drops, and Particles. Academic Press, New York.

Ghiaasiaan, S.M., 2003. Gas–liquid two-phase flow and boiling in mini and microchannels. Multiphase Sci. Tech. 15, 323–336.

Gibson, A.H., 1913. On the motion of long air-bubbles in a vertical tube. Philos. Mag. 26, 952–965.

Hibiki, T., Ishii, M., 2000a. One-group interfacial area transport of bubbly flows in vertical round tubes. Int. J. Heat Mass Transfer 43, 2711–2726.

Hibiki, T., Ishii, M., 2000b. Two-group interfacial area transport equations at bubbly-to-slug flow transition. Nucl. Eng. Des. 202, 39–76.

Hibiki, T., Ishii, M., 2001. Interfacial area concentration in steady fully developed bubbly flow. Int. J. Heat Mass Transfer 44, 3443–3461.

Hibiki, T., Ishii, M., 2002a. Interfacial area concentration of bubbly flow systems. Chem. Eng. Sci. 57, 3967–3977.

Hibiki, T., Ishii, M., 2002b. Distribution parameter and drift velocity of drift-flux model in bubbly flow. Int. J. Heat Mass Transfer 45, 707–721.

Hibiki, T., Ishii, M., 2002c. Development of one-group interfacial area transport equation in bubbly flow systems. Int. J. Heat Mass Transfer 45, 2351–2372.

Hibiki, T., Ishii, M., 2003. One-dimensional drift-flux model and constitutive equations for relative motion between phases in various two-phase flow regimes. Int. J. Heat Mass Transfer 46, 4935–4948, Erratum published in Int. J. Heat Mass Transfer 48, 1222–1223.

Hibiki, T., Hogsett, S., Ishii, M., 1998. Local measurement of interfacial area, interfacial velocity and liquid turbulence in two-phase flow. Nucl. Eng. Des. 184, 287–304.

Hibiki, T., Situ, R., Mi, Y., Ishii, M., 2003. Local flow measurements of vertical upward bubbly flow in an annulus. Int. J. Heat Mass Transfer 46, 1479–1496.

Hibiki, T., Goda, H., Kim, S., Ishii, M., Uhle, J., 2004. Structure of vertical downward bubbly flow. Int. J. Heat Mass Transfer 47, 1847–1862.

Hibiki, T., Lee, T.H., Lee, J.Y., Ishii, M., 2006. Interfacial area concentration in boiling bubbly flow systems. Chem. Eng. Sci. (doi:10.1016/j.ces.2006.09.009).

Ishii, M., 1977. One-dimensional Drift-flux Model and Constitutive Equations for Relative Motion between Phases in Various Two-phase Flow Regimes. ANL-77-47.

Ishii, M., Hibiki, T., 2005. Thermo-fluid Dynamics of Two-phase Flow. Springer.

Ishii, M., Mishima, K., 1984. Two-fluid model and hydrodynamic constitutive relations. Nucl. Eng. Des. 82, 107–126.

Kandlikar, S.G., 2002a. Two-phase flow patterns, pressure drop, and heat transfer during boiling in minichannel flow passages of compact evaporators. Heat Transfer Eng. 23, 5–23.

Kandlikar, S.G., 2002b. Fundamental issues related to flow boiling in minichannels and microchannels. Exp. Thermal Fluid Sci. 26, 389–407.

Kawaji, M., Chung, P.M.Y., 2004. Adiabatic gas–liquid flow in microchannles. Microscale Thermophys. Eng. 8, 239–257.

Lee, H.J., Lee, S.Y., 2001a. Pressure drop correlations for two-phase flow within horizontal rectangular channels with small heights. Int. J. Multiphase Flow 27, 783–796.

Lee, H.J., Lee, S.Y., 2001b. Heat transfer correlation for boiling flows in small rectangular horizontal channels with low aspect ratios. Int. J. Multiphase Flow 27, 2043–2062.

Lockhart, R.W., Martinelli, R.C., 1949. Proposed correlation of data for isothermal two-phase, two-component flow in pipes. Chem. Eng. Prog. 5, 39–48.

Mishima, K., Hibiki, T., 1996. Some characteristics of air–water two-phase flow in small diameter vertical tubes. Int. J. Multiphase Flow 22, 703–712.

Ohta, H., 2005. Boiling and two-phase flow in channels with extremely small diameters: a review of Japanese research. Microfluidics Nanofluidics 1, 94–107.

Oolman, T., Blanch, W.H., 1986. Bubble coalescence in air-sparged bioreactors. Biotechnol. Bioeng. 28, 578–584.

Qu, W.L., Mudawar, I., 2003. Measurement and prediction of pressure drop in two-phase micro-channel heat sinks. Int. J. Heat Mass Transfer 46, 2737–2753.

Serizawa, A., Feng, Z.P., Kawahara, Z., 2002. Two-phase flow in microchannels. Exp. Therm. Fluid Sci. 26, 703–714.

Sleicher Jr., C.A., 1962. Maximum stable droplet size in turbulent flow. AIChE J. 8, 471–477.

Takamasa, T., Goto, T., Hibiki, T., Ishii, M., 2003. Experimental study of interfacial area transport of bubbly flow in small-diameter tube. Int. J. Multiphase Flow 29, 291–304.

Tomiyama, A., Kataoka, I., Zun, I., Sakaguchi, T., 1998. Drag coefficients of single bubbles under normal and microgravity conditions. JSME Int. Ser. B 41, 472–479.

Wu, Q., Ishii, M., 1999. Sensitivity study on double-sensor conductivity probe for the measurement of interfacial area concentration in bubbly flow. Int. J. Multiphase Flow 25, 155–173.

Zhang, W., Hibiki, T., Mishima, K., 2004. Correlation for flow boiling heat transfer in mini-channels. Int. J. Heat Mass Transfer 47, 5749–5763.

Zhang, W., Hibiki, T., Mishima, K., 2005. Correlation for flow boiling heat transfer at low liquid Reynolds number in small diameter channels. J. Heat Transfer 127, 1214–1221.

Zhang, W., Hibiki, T., Mishima, K., 2006. Correlation of critical heat flux for flow boiling of water in mini-channels. Int. J. Heat Mass Transfer 49, 1058–1072.

Zuber, N., Findlay, J.A., 1965. Average volumetric concentration in two-phase flow systems. J. Heat Transfer 87, 453–468.

Zun, I., 1988. Transition from wall void peaking to core void peaking in turbulent bubbly flow. Transient Phenomena in Multiphase Flow. Hemisphere, Washington, DC, pp. 225–245.